Nationaal Lucht- en Ruimtevaartlaboratorium
National Aerospace Laboratory NLR

NLR-TP-2002-496

Numerical prediction capabilities and analysis of flow development for a supersonic civil transport at low speed

J. van Muijden and A. Elsenaar

Nationaal Lucht- en Ruimtevaartlaboratorium
National Aerospace Laboratory NLR

NLR-TP-2002-496

Numerical prediction capabilities and analysis of flow development for a supersonic civil transport at low speed

J. van Muijden and A. Elsenaar

This report is based on a presentation held at the CEAS Conference, Cambridge UK, 10-12 June 2002

Customer:	National Aerospace Laboratory NLR
Working Plan number:	A.1.A.4
Owner:	National Aerospace Laboratory NLR
Division:	Fluid Dynamics
Distribution:	Unlimited
Classification title:	Unclassified
	September 2002

Summary

This paper focuses on two issues. First, it describes the application of present-day multi-block structured CFD-tools to the analysis of flow development and prediction of aerodynamic coefficients of a supersonic civil transport (SCT) with leading-edge flap deflections at low-speed conditions. Second, the flow development with incidence and separation onset is studied to obtain a better understanding of the type of flow under consideration.

The numerical study of the flow around this configuration is based on solution of the Navier-Stokes equations in combination with a two-equation k-ω turbulence model employing specific modifications for vortex-dominated flow. The flow conditions examined range between 6 and 12 degrees incidence, at a Mach number of 0.25 and a Reynolds number of 7.3 million, based on mean aerodynamic chord. Different meshes have been used to assess the dependency of flow solutions on mesh density. Comparison with experimental data and industrial accuracy requirements is performed, from which indications for minimum mesh density are derived.

The study of flow development with incidence is based on experimental oil flow patterns, pressure distributions and aerodynamic coefficients, supplemented with flow field and surface data from the CFD-solutions.

It is concluded that the low-speed aerodynamic characteristics for attached as well as separated flow on an SCT with deflected leading-edge flaps can be predicted with acceptable accuracy, in accordance with industrial accuracy requirements. This allows the presented method to be applied in further computational studies regarding the improvement of low-speed characteristics of SCT.

List of Symbols

b	Wing span
C_D	Drag Coefficient
C_L	Lift coefficient
C_M	Pitching moment coefficient
h	Relative mesh size
y	Spanwise coordinate
ŭ	Incidence
φ	Increment
ɥ = 2y/b	Nondimensional span coordinate
# cells	Number of cells

Contents

(36 pages in total)

This page is intentionally left blank

1 Introduction

One critical technology problem related to the viability and environmental acceptability of a second-generation supersonic civil transport (SCT) is encountered at take-off and fly-over conditions. At such conditions, compliance with future community noise and emissions regulations will play an increasingly important role in the operation of SCT from existing international airports. This issue has been addressed in NASA's high-speed research programme (Ref 1) as well as in European SCT-research programmes (Refs 2, 3). One of the approaches towards a solution, apart from engine cycle design, is sought in a major improvement of the aerodynamic efficiency (lift-to-drag ratio) at low-speed conditions. This will immediately reduce the engine thrust required leading to reductions of noise as well as emissions.

Within the EUROSUP project (Ref 2), a basic low-speed SCT design has been established by applying leading-edge flap deflections to the supersonic wing shape in a manual design approach. Though reasonably successful in meeting the EUROSUP low-speed design target (L/D=8) the resulting configuration exhibits largely separated flow at the design point, indicating that further drag reductions might be possible. It has been concluded that further computational and experimental research in this area is needed to improve the aerodynamic efficiency at the low-speed design condition.

The low-speed SCT-research has been continued after the end of the EUROSUP project. Initial investigations were executed in a GARTEUR action group, which was active during 1999 in the period between EUROSUP and its follow-up programme EPISTLE (Ref 3). The EPISTLE project is aiming at a further reduction of flow separations, thereby reducing drag and improving the low-speed lift-to-drag ratio by an additional 15 to 20 percent.

In order to verify and validate the CFD-tools that are needed in a sensitivity-based design approach at low-speed conditions, the EPISTLE project revisited the EUROSUP low-speed configuration. Additional measurements were performed in the DNW-HST wind tunnel in Amsterdam to resolve remaining questions concerning flow development with incidence and transition strip influences. Navier-Stokes based CFD-computations were performed to validate the flow solvers for the specific type of flow under consideration. For this purpose, industrial accuracy requirements were formulated that have to be met.

In the following, the prediction of flow development with incidence is analysed, using the experimental database as a reference. The items addressed include: aerodynamic coefficient and pressure distribution comparisons, prediction of separation onset, analysis of topological flow

structure with incidence, and numerical aspects like mesh density and turbulence model influences.

The purpose of this paper is to identify the requirements needed for CFD-based flow analysis to obtain reasonable predictions of the essential flow phenomena and a reliable prediction of the aerodynamic coefficients for an SCT-configuration with partially separated flow. These requirements are needed prior to application of the CFD-tools in forthcoming analysis and design tasks.

2 Configuration

The wind tunnel model of the present SCT-configuration consists of a sting-mounted fuselage with three exchangeable wings representing the supersonic, transonic and low-speed wing designs. Fig 1 clearly shows the low-speed wing with its deflected leading-edge flaps. Along the wing span, three flap segments were defined, each having its own deflection. A continuous geometry was obtained by applying an s-shaped transition region over a small fraction of span between two adjacent flap segments. This approach guarantees that a multi-block structured CFD-approach remains possible. Furthermore, the fuselage and sting were modelled in the computational meshes as an extended fuselage without cross-sectional dimension changes.

Fig 1 Wind tunnel model of low-speed configuration, showing deflected leading-edge flaps

3 Industrial accuracy requirements

The application of flap systems on an SCT has been studied in the past to improve the low-speed performance of Concorde. Though never actually applied, the results of these studies still form the basis of present-day investigations. An overview of attainable improvements in aerodynamic efficiency and noise is given in Ref 4.

Accuracy requirements have been formulated by industry that have to be met by CFD-tools applied in analysis and design tasks. The purpose of meeting the accuracy requirements is to reduce the uncertainty in computed flow solutions including partially separated flow for newly designed configurations. As such, the risk of selecting a sub-optimal design for wind tunnel testing later on in the project is reduced. The accuracy requirements have been derived from a parameter study using a project optimisation tool that links drag variations to noise reductions and were supplied as:
qpU± 0.5 degrees,
qpC_D ± 17 drag counts (one drag count equals 0.0001 in C_D),
qpC_M ± 0.0035.
It is stressed that these accuracy requirements were issued for largely attached flow, although the ranges mentioned above are also used as indications at flow conditions including separation.

4 Flow solver

The flow solver employed in the present study is part of the NLR-developed multi-block structured CFD-system ENFLOW (Ref 5). The system consists of a domain modeller to create a subdivision of the flow domain into blocks, a grid generator to obtain the block-structured meshes, and a flow solver that can be applied in Euler or Navier-Stokes mode. The flow solver can be applied to steady as well as time-dependent flow problems. In Navier-Stokes mode, the full Reynolds-averaged Navier-Stokes equations or the thin-layer approximations thereof can be solved. A number of optional turbulence models are available. Besides the standard Baldwin-Lomax algebraic turbulence model, the two-equation k-Y turbulence model including specific modifications to reduce the free-stream turbulence intensity dependence and to correct the levels of turbulent viscosity inside vortex cores (Ref 6) is often used. An additional optional turbulence model is the explicit algebraic Reynolds stress model (EARSM).

In the present study, use has been made of the full Reynolds-averaged Navier-Stokes equations, in combination with the two-equation k-Y turbulence model including the NLR-specific modifications.

5 Computational meshes

An initial common mesh was available at the start of the validation exercise, based on a C-O type block-topology (C-O indicating a C-type topology chordwise and O-type spanwise). This mesh contains 793,872 cells. Previous CFD-experience indicated that meshes of this density yield a reasonable prediction of aerodynamic coefficients when using the Baldwin-Lomax turbulence model with Degani-Schiff modification for vortex-dominated flow. In the present study, however, it was felt that the computation of separation onset and vortical flow development requires a more generally applicable turbulence model, for which the two-equation k-ϒ model has been selected. Using this turbulence model, the requirements on mesh density are more severe, as will be shown in the comparison of aerodynamic coefficients.

A new basic mesh was created in an O-O type block-topology, generated by semi-automatic tools for domain decomposition (Ref 7). The basic mesh contains 1,543,168 cells in 102 blocks. By increasing the number of cells in each direction with a factor of 1.5, a fine mesh with 5,208,192 cells was obtained. These two meshes and their sublevels have been used to obtain flow solutions and indications of mesh density dependencies of aerodynamic coefficients.

Semi-automatic tools for domain-decomposition are most satisfactorily applied when an O-type mesh around the wing trailing edge is adopted, since it allows for an easy “blow-up” approach of the surface to create the first layer of boundary-layer blocks. Besides that, O-type meshes are efficient in the sense of avoiding the occurrence of boundary-layer resolutions away from solid walls. The present application, being one of the first configurations to be tested with an O-O type block-topology for viscous computations, has been checked with a few Navier-Stokes solutions obtained on a more conventional fine mesh. The previously used fine mesh for the transonic configuration (Ref 8), containing 3,168,256 cells, has been adjusted to the present low-speed wing shape for these verification purposes.

6 Convergence characteristics

The computed flow around the low-speed SCT-configuration is fully attached at 6 degrees incidence, and contains partially separated flow including several distinct vortices at higher incidences. The increasing complexity of the flow field with incidence is reflected in the convergence behaviour of the flow solver. For fully attached flow, computations were performed using a full multi-grid approach. This, in general, leads rapidly to converged aerodynamic coefficients and three orders of magnitude reduction of flow equation residuals. In the initial phase of the computations on a coarse mesh level, severe oscillations in aerodynamic

coefficients occur which are typical for these low-Mach number flows. Good convergence behaviour is no longer standard on fine meshes in combination with partially separated flow. Good convergence is still obtained on the basic mesh of 1.5 million cells, at the cost of additional iterations and a reduction of the number of mesh levels used in the multi-grid process. On the fine mesh of 5.2 million cells, less satisfactory convergence behaviour is found. Aerodynamic coefficients show an oscillatory behaviour which damps only slowly, while flow equation residuals tend to decrease at a very low rate. As a result, many iterations are mandatory. It is believed that steady-state solutions for separated flow on fine meshes are difficult to obtain due to difficult flow physics of multiple interacting vortices. It has been indicated within EPISTLE (see Ref 3) that performing time-accurate computations is another approach to reach a converged state for such flow conditions.

7 Mesh refinement effects on coefficients

An overview is presented to analyse the effects of mesh density on the flow solutions. For this purpose, use is made of the flow solutions at 6 and 10 degrees incidence on the available meshes of varying density.

At first, the variation of drag is studied in relation to the mesh density. For this purpose, the relative mesh size h is introduced, defined by

$$h = \sqrt[3]{\#cells\,reference\,mesh / \#cells\,actual\,mesh}$$

which gives a numerical value for the average number of cells in each coordinate direction relative to the average number of cells in each coordinate direction of the reference mesh. Here, the fine mesh having 5.2 million cells is chosen as the reference mesh. This fine mesh then has, by definition, a relative mesh size h=1. Sublevels of this mesh, obtained by leaving out every other mesh point, will have a relative mesh size of h=2, h=4, and so on. The relative mesh sizes of the different meshes are given in Table 1.

Table 1 Relative mesh sizes of the meshes

mesh	h - fine level	h - sublevels
O-O, 5.2 Mcells	1.00	2.00, 4.00
C-H, 3.2 Mcells	1.18	2.36, 4.72
O-O, 1.5 Mcells	1.50	3.00, 6.00
C-O, 0.8 Mcells	1.87	Not used

The relative mesh size is now used to plot the computed drag coefficient as a function of mesh density. In Fig 2, the drag values as obtained on the different meshes at 6 degrees incidence are shown. The horizontal axis of this figure ranges between zero (vanishing mesh size) and 4.8, which correlates with a very coarse mesh of only 47,094 cells. It is shown that, for this attached flow case, the variations of drag with increasing mesh density exhibits an orderly behaviour within each type of mesh. Following Ref 9, an extrapolation is applied to obtain an estimated drag coefficient for vanishing mesh size. Such an extrapolation can be applied successfully only if the meshes on which the extrapolating curve is based are sufficiently fine, and all flow solutions used are sufficiently converged.

Here, a quadratic curve is used, based on the three results obtained on the finest available mesh levels of a particular type of mesh, to perform the extrapolation. This is based on the notion that the local accuracy of the numerical scheme is a mix of first- and second-order terms that introduce respectively a linear and a quadratic dependency on the relative mesh size. This procedure has been applied succesfully in the past (Refs 8, 9). In Fig 2, the extrapolation based on the O-O type meshes yields a drag value within 5 counts from the experimental value. The remaining difference, as explained earlier, might be attributed to the assumed fully turbulent boundary layer in the computations, whereas in the experiment some small regions of laminar flow on wing and fuselage are present ahead of the transition strips. A second extrapolation using the results obtained on the C-H type meshes, though partially based on a very coarse mesh level (h=4.72), still results in an acceptable extrapolated drag value.

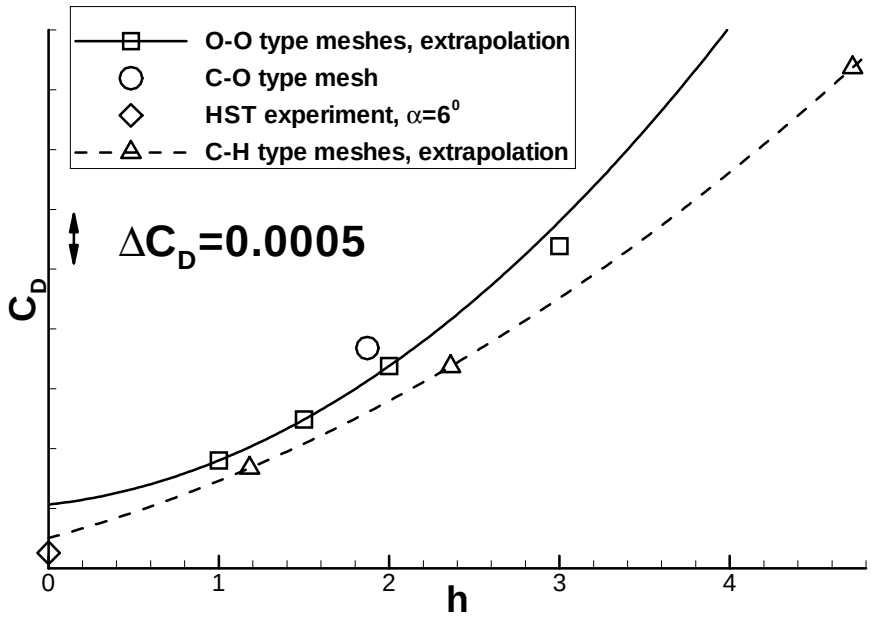

Fig 2 Drag coefficient versus h, Ŭ = 6 degrees

The drag coefficients at 10 degrees incidence are depicted in Fig 3. The situation is completely different for these flow conditions including severe separations. All computed drag values are much higher than the experimental value, in the order of 40 drag counts or more (at 6 degrees incidence this difference is about 8 drag counts or more). Applying the extrapolation procedure to these data will not lead to plausible results for vanishing mesh size, since the computed values on the fine meshes will differ too much from the extrapolated values (in the order of tens of drag counts). The difficulties of performing a plausible extrapolation for separated flow can be attributed to the modest convergence obtained on especially the finest meshes on the one hand, while also the appearance of more and more flow details with mesh refinement does not yield a very orderly behaviour of drag dependency on mesh density as for the attached flow cases.

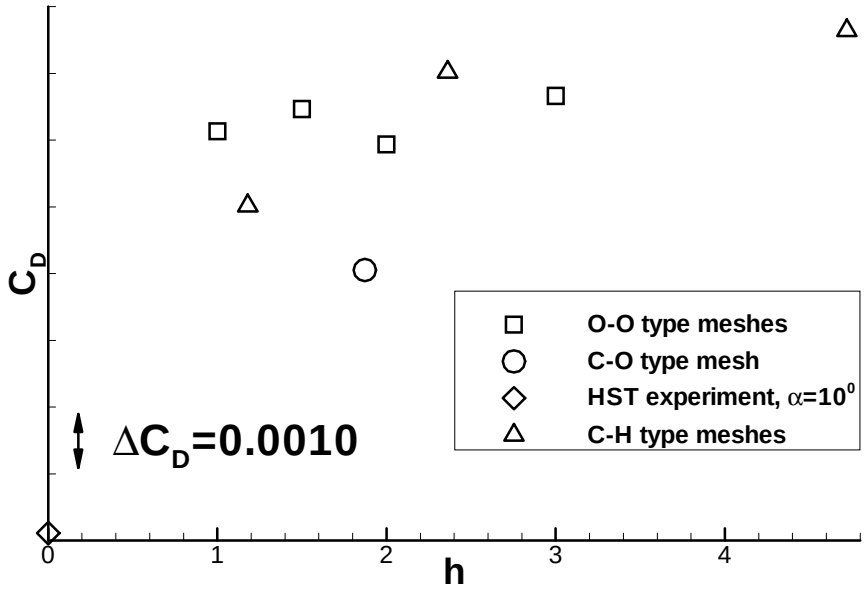

Fig 3 Drag coefficient versus h, Ŭ = 10 degrees

8 Mesh refinement effects on total pressure losses

An analysis of the total pressure losses behind the wing trailing edge, obtained on the different meshes, is now shown for further interpretation of mesh influences. For the attached flow case at 6 degrees incidence, the results as obtained on the different meshes are shown in Figs 4-7. The main difference observed is the increase in total pressure loss within the tip vortex, which is captured better on finer meshes having an O-type topology at the wing tip. An exception is the mesh with 3.2 million cells, possessing an H-type topology at the wing tip. The tip vortex on this mesh is not in line with expectations based on relative mesh density, simply because the tip

is not properly rounded by the mesh. Other influences of the different mesh topologies on the flow solutions are rather limited.

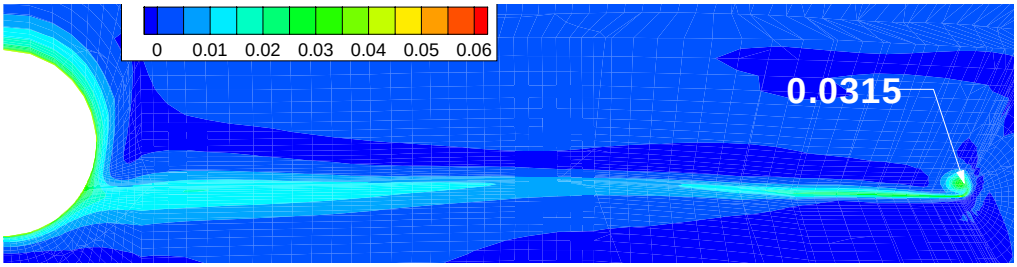

Fig 4 Total pressure losses behind trailing edge, C-O mesh, 0.8 million cells, 6 degrees incidence

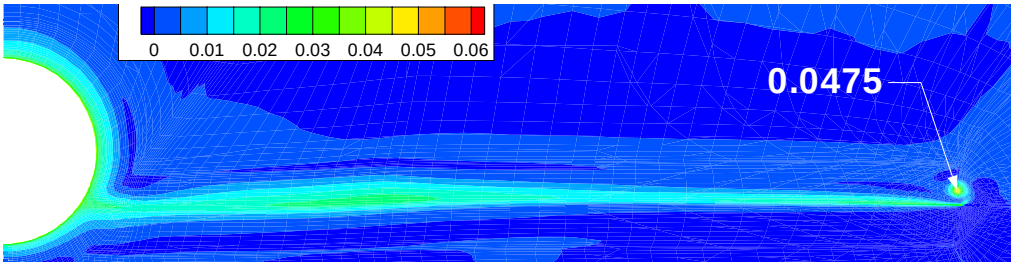

Fig 5 Total pressure losses behind trailing edge, O-O mesh, 1.5 million cells, 6 degrees incidence

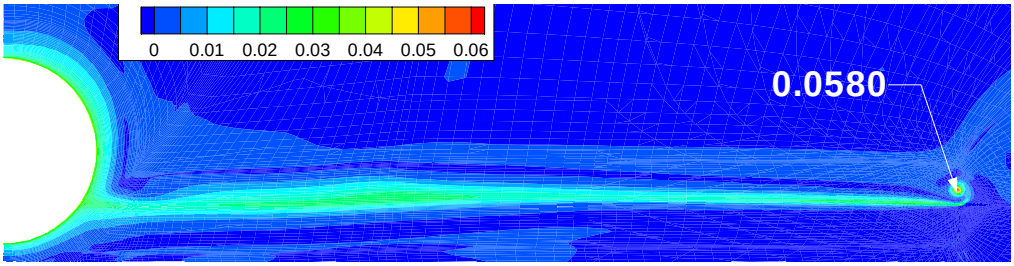

Fig 6 Total pressure losses behind trailing edge, O-O mesh, 5.2 million cells, 6 degrees incidence

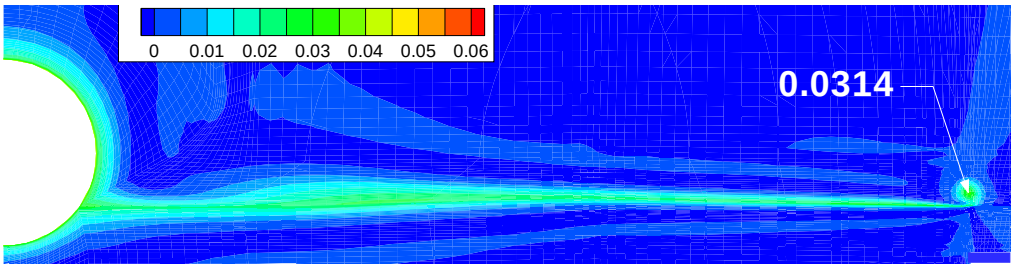

Fig 7 Total pressure losses behind trailing edge, C-H mesh, 3.2 million cells, 6 degrees incidence

At 10 degrees incidence, the dependency on mesh density and topology is, as expected, much larger (Figs 8-11). The global vortical structures are predicted on each of the meshes, but the details differ considerably, especially with respect to the position of the vortex on the outboard wing. It is observed that mesh refinement within a particular block-topology leads to more details without changing the position of the vortices (Figs 9, 10). Both alternative block-topologies lead to slightly different positions of the inboard vortex, whereas especially the C-H type block topology appears to influence the solution on the outboard wing. While there appear to be two distinct vortices on the outboard wing in Fig 11, the other meshes show a stronger, combined vortex closer to the wing tip. As will be shown in the comparison with experimental data, the position of the outboard wing vortex on the O-O type meshes appears to be too close to the wing tip.

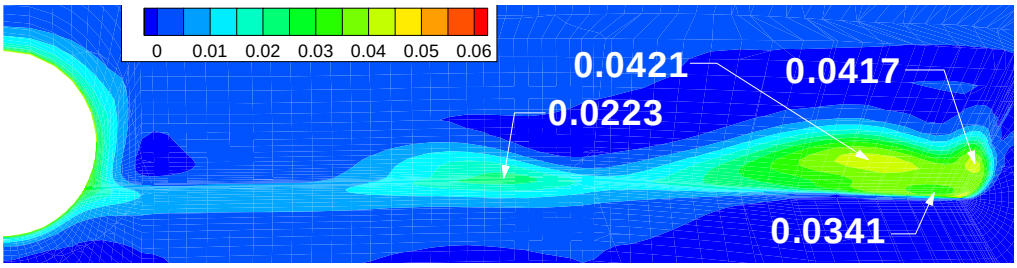

Fig 8 Total pressure losses behind trailing edge, C-O mesh, 0.8 million cells, 10 degrees incidence

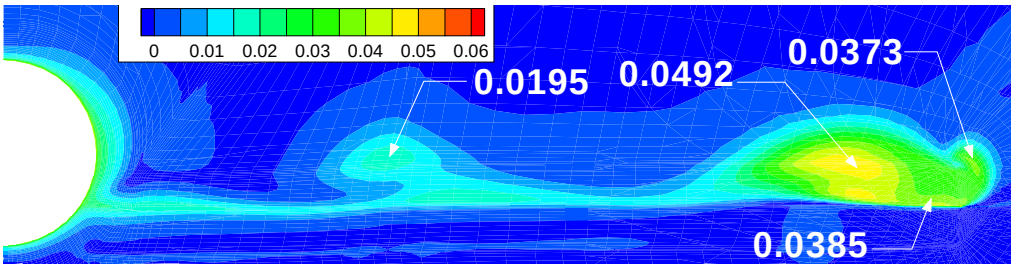

Fig 9 Total pressure losses behind trailing edge, O-O mesh, 1.5 million cells, 10 degrees incidence

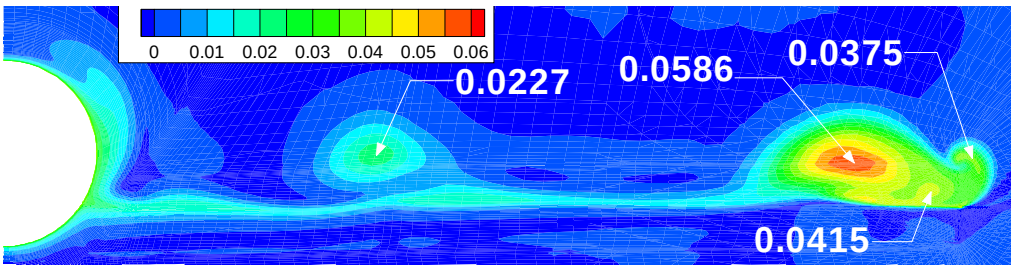

Fig 10 Total pressure losses behind trailing edge, O-O mesh, 5.2 million cells, 10 degrees incidence

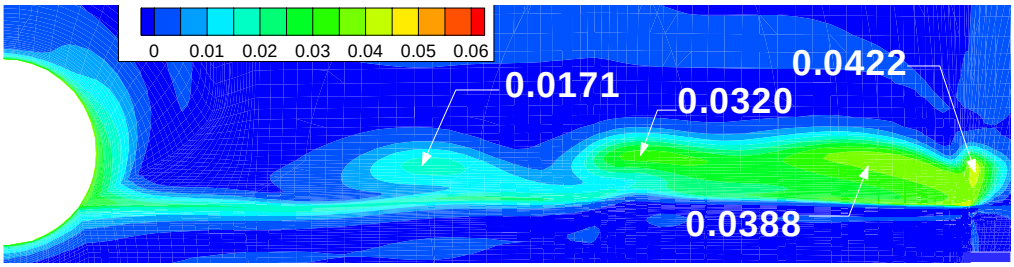

Fig 11 Total pressure losses behind trailing edge, C-H mesh, 3.2 million cells, 10 degrees incidence

9 Experimental observations

The SCT configuration has been tested in the DNW-HST high speed wind tunnel at supersonic, transonic and low-speed conditions. The low-speed configuration, with deflected leading edge, was tested at 4 bar stagnation pressure at a Reynolds number (based on mean aerodynamic chord) of about 7 million. During the EUROSUP program oil flow pictures have been made at 10 degrees incidence. For the EPISTLE tests oil flow visualizations have been made for 5, 6, 8 and 10.5 degrees. During the tests, pressures in chordwise direction on three stations (29, 52 and 71% of half span) have been measured as well. The EPISTLE and EUROSUP tests differed in transition fixation following a more in-depth transition study that resulted in the adaptation of a transition strip on upper and lower surface close to and parallel all along the leading edge. These differences affected the drag near the optimum L/D up till 7 degrees incidence. There are no significant effects of the transition strips above 7 degrees, which is the most interesting part as far as flow development is concerned.

In Fig 12a the observed oil flow pattern at 10.5 degrees has been presented, while the outer wing oil flow pattern at 10 degrees is shown in Fig 12b.

Fig 12a Oil flow visualisation at Ŭ=10.5 degrees

Fig 12b Outer wing oil flow visualisation at Ŭ=10 degrees

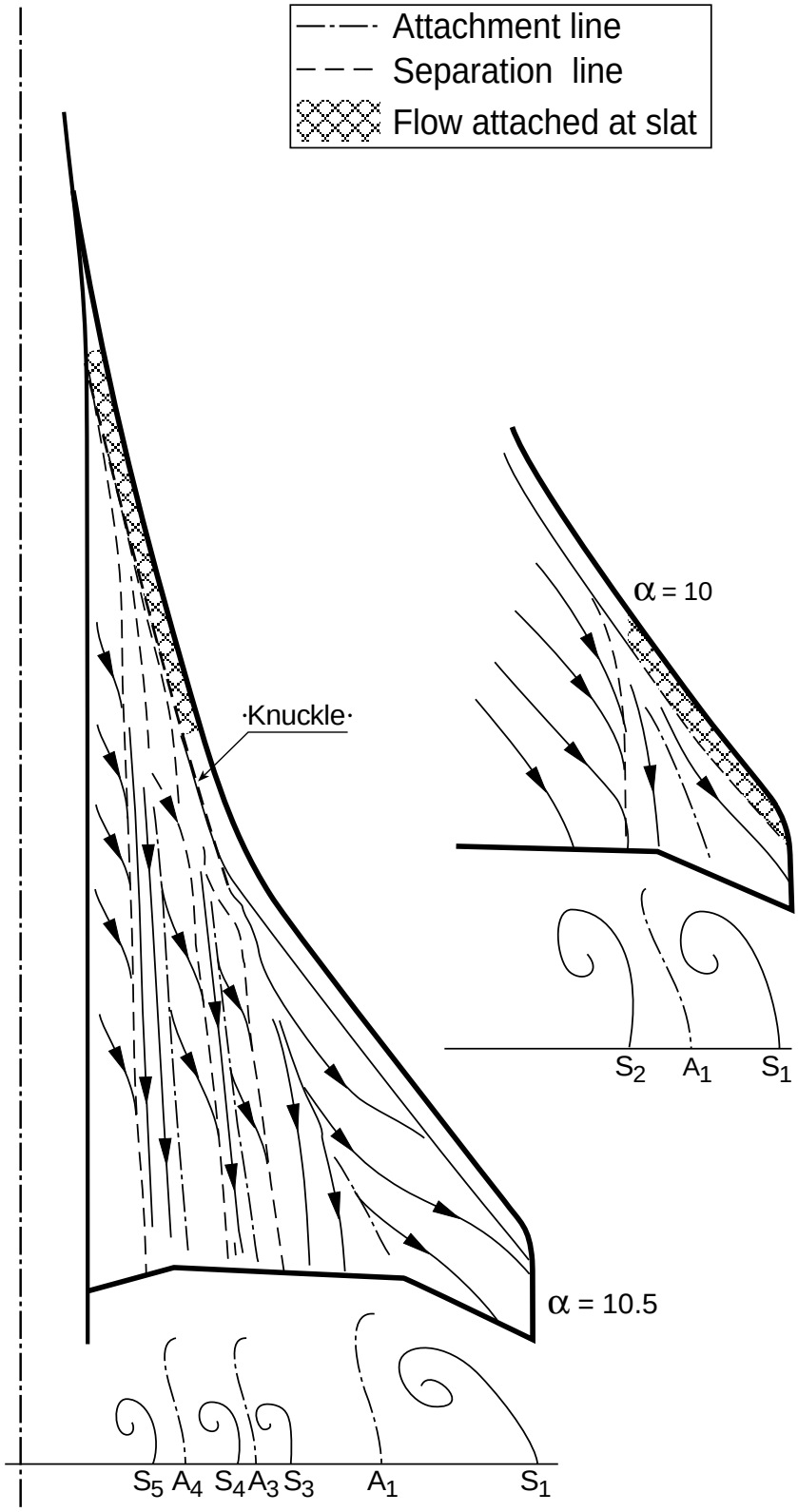

Fig 13 Tentative interpretation of oil flow at Ŭ=10.5 degrees (left) and at 10 degrees (right, outer wing)

A tentative interpretation of this flow is presented in Fig 13. This is essentially the same as the interpretation discussed in Ref 10, though there made at 10 degrees incidence. The interpretation of surface flow near the wing tip for the latter case is given in the insert of Fig 13 and will be discussed later. In the same figure also a tentative topological interpretation in a cross flow plane behind the wing is presented. The main features of the configuration and related flow developments are:

- complex geometry: variations in leading-edge and trailing-edge sweep, deflected leading-edge flap with a slope discontinuity between flap and main wing (the ‘knuckle’); it is to be noted, but not clearly visible, that the flap consists of a number of straight segments each having its own deflection angle, which in principle causes slope discontinuities at their junction (in the present study slightly smoothed out);
- the flow is a mixture of attached and separated flow regions: at 10.5 degrees incidence only the flow on the inboard flap is still attached, but at a slightly lower incidence of 10 degrees also the outboard flap indicates attached flow, with separation starting from the ‘knuckle’; in between the flow is separated right from the leading edge;
- there are multiple streamwise vortices that originate at the leading-edge or ‘knuckle’ separation but are subsequently turned into streamwise direction; these vortices are not directly visible in the oil flow , but the related separation lines (where oil is accumulated) are clearly visible; the change in flow topology on the outboard wing for a small change in incidence is to be noted.

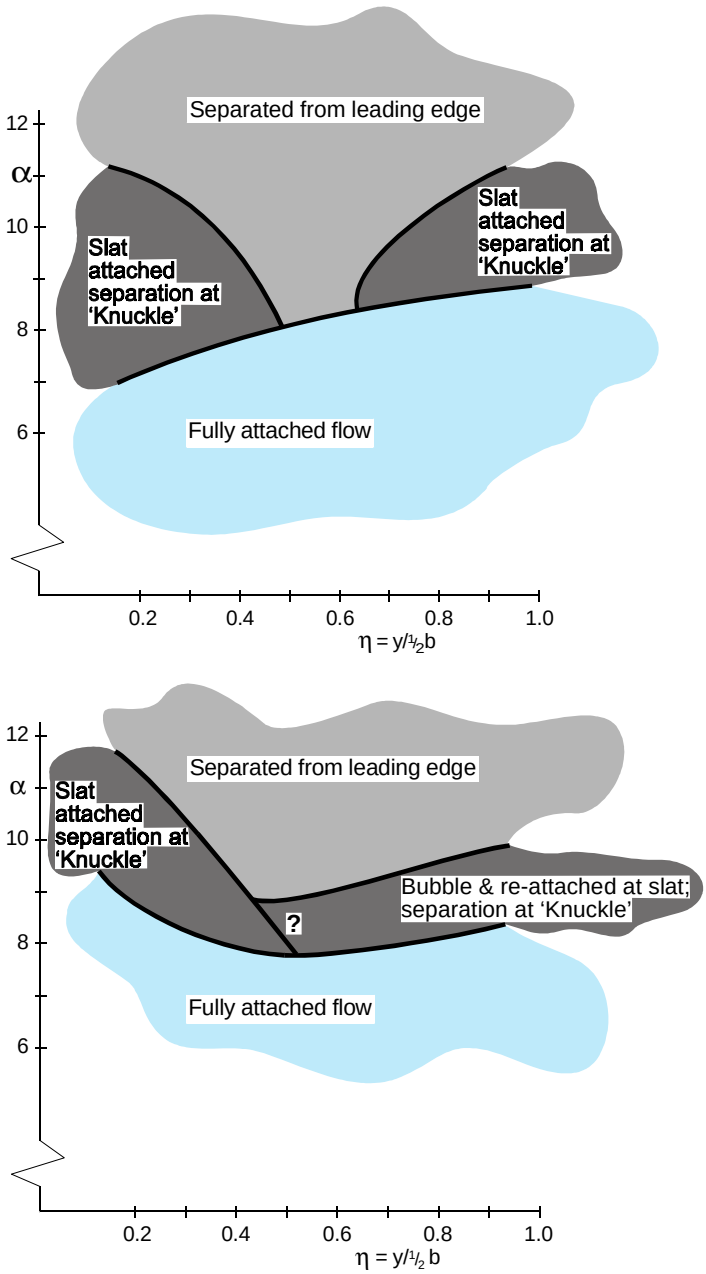

Fig 14 Tentative interpretation of flow development with incidence, experiment (top) versus CFD (bottom)

In Fig 14 it has been attempted to sketch the flow development as function of incidence. At 10 degrees (EUROSUP) and 10.5 degrees incidence (EPISTLE) detailed oil flow pictures were available. By scrutinising the developments of the pressure distributions, in particular in the leading-edge region, a (somewhat subjective) distinction can be made between attached and separated flow and the related vortex formation.

10 Comparison with CFD calculations: separation development

In aircraft design CFD calculations are primarily used to optimise and define the wing shape. In this particular example the requirement is to reduce drag at a particular lift coefficient (for 'climb-out'), a flow condition where flow separation and vortex formation are likely to be present. Hence, a challenging requirement for CFD-based flow analysis in this case is the ability to predict these effects.

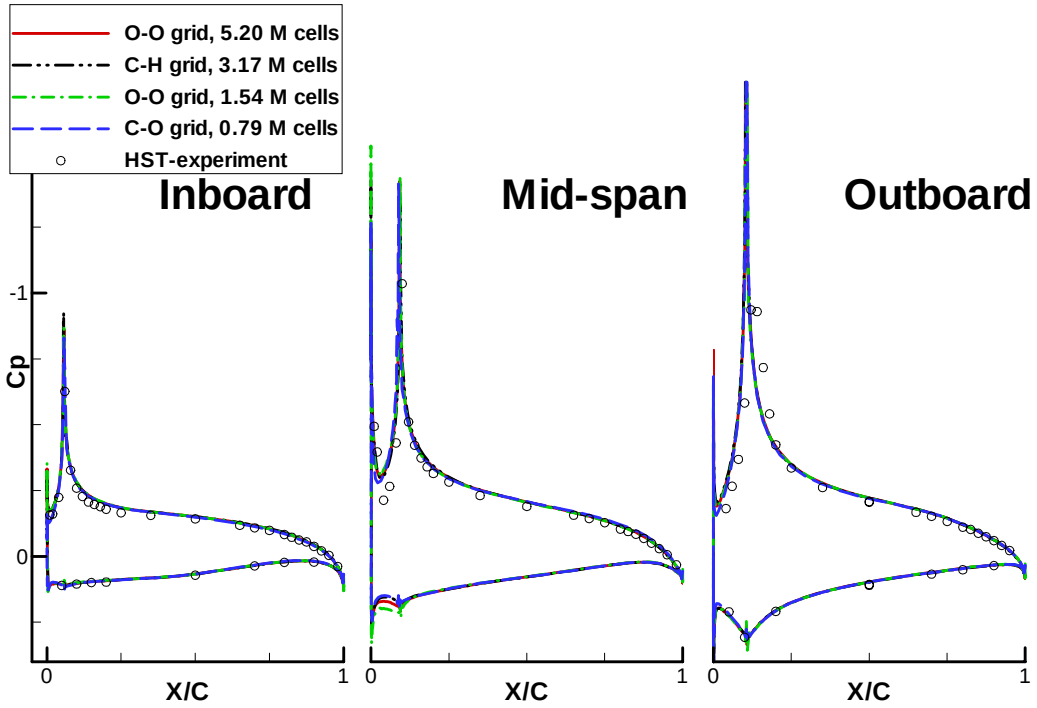

Fig 15 Pressure distribution, Ŭ = 6 degrees

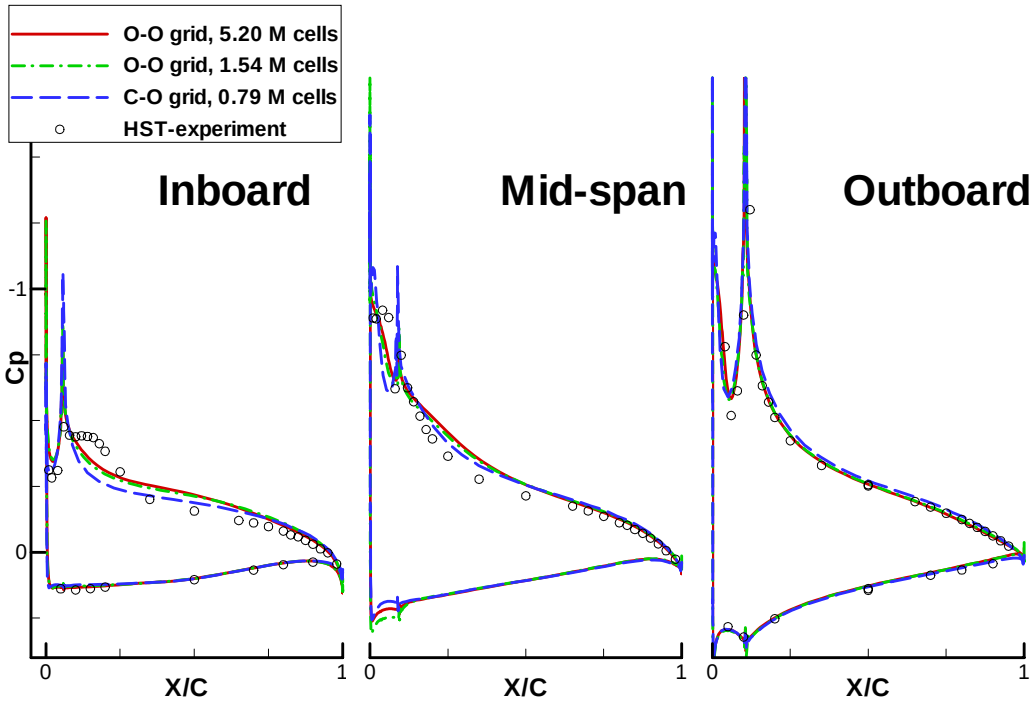

Fig 16 Pressure distribution, Ŭ = 8 degrees

Fig 15 shows such a comparison of the pressure distribution for fully attached flow near the optimum in L/D (Ŭ=6 degrees). The solutions on the various grids hardly differ from each other and agree well with the experiment. A similar situation is found at 8 degrees incidence (Fig 16) but there are already differences in the leading-edge region: at the inboard station the separation at the 'knuckle' is not captured and at mid-span the situation is a bit confusing, with indications of leading-edge separation in theory and experiment. The CFD skin friction lines for this case (Fig 17) clearly indicate for the mid-span and outboard wing a separation bubble starting at the leading edge and reattaching on the flap surface itself. In the experiment at the mid-span position the situation is confusing, but the experimental oil flow suggests that the flow is attached at the outer wing including the slat. This different behaviour is not clearly understood and requires more attention in CFD and experiment.

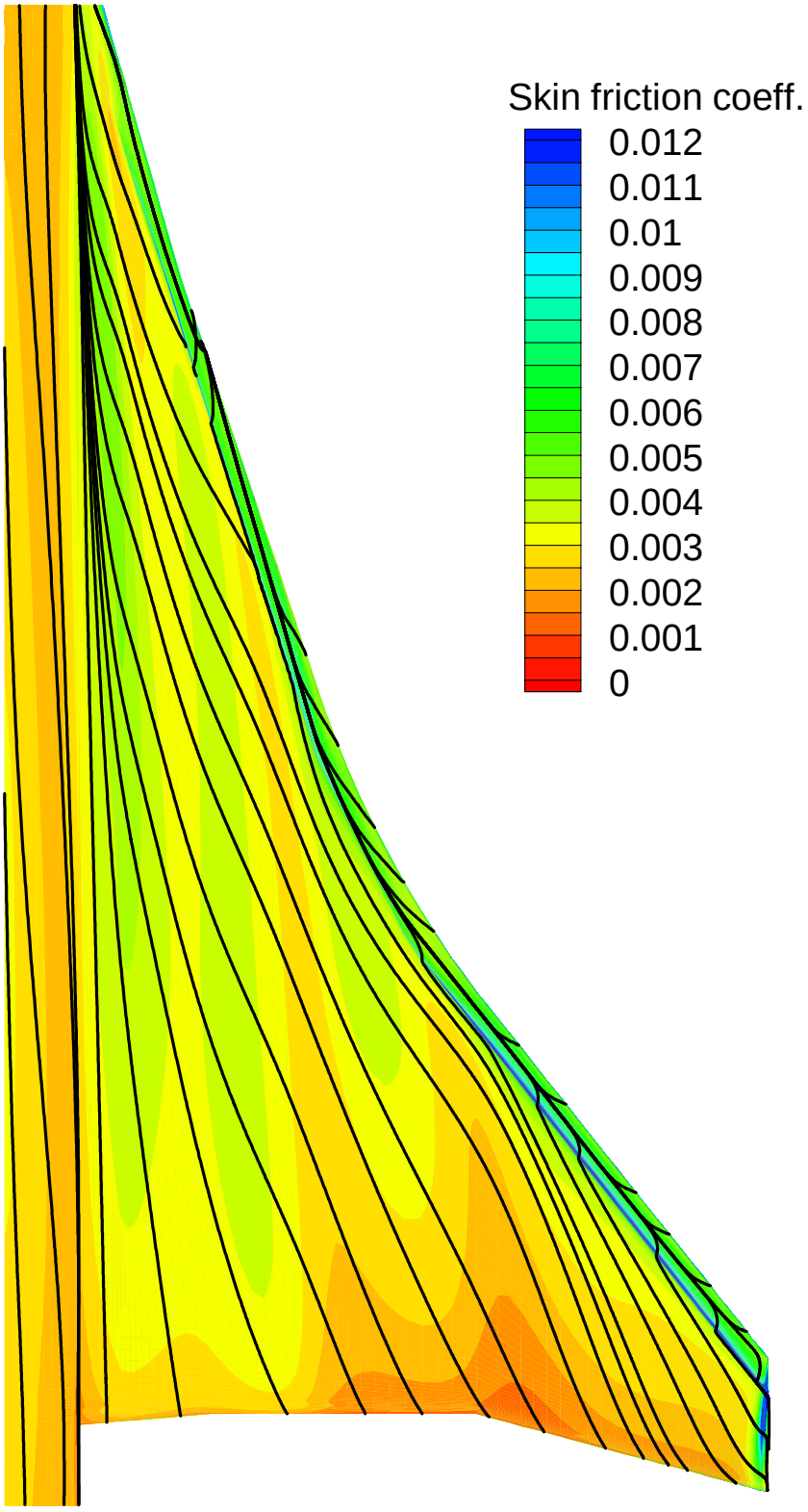

Fig 17 Skin friction lines at 8 degrees incidence

At higher incidences (Figs 18, 19, 20 and 21) the differences between the various CFD solutions and with the experiment become much larger, notably on the outer wing. In the experiment, vortex formation at the leading edge starts at mid-span and develops rapidly in outboard direction: note the change between 10 and 10.5 degrees incidence. This change is also reflected in the oil flow and its interpretation as already presented in Figs 12 and 13. Fig 22, taken from the EUROSUP results, illustrates the same development over a larger range of incidences. It appears that in the CFD calculations, this outboard movement of the vortex is predicted much earlier and with a stronger vortex. CFD-results also show a relatively large mesh dependency for these cases. The corresponding CFD skin friction lines as shown in Fig 23 (including an indication of the magnitude of the skin friction coefficient) further illustrate this. The areas with high skin friction can be found at the inboard leading-edge flap and underneath the two vortices that originate at the wing root and at mid-span. At even higher lift values all separations originate at the leading edge and it is expected that at these cases one or two dominant vortices will result.

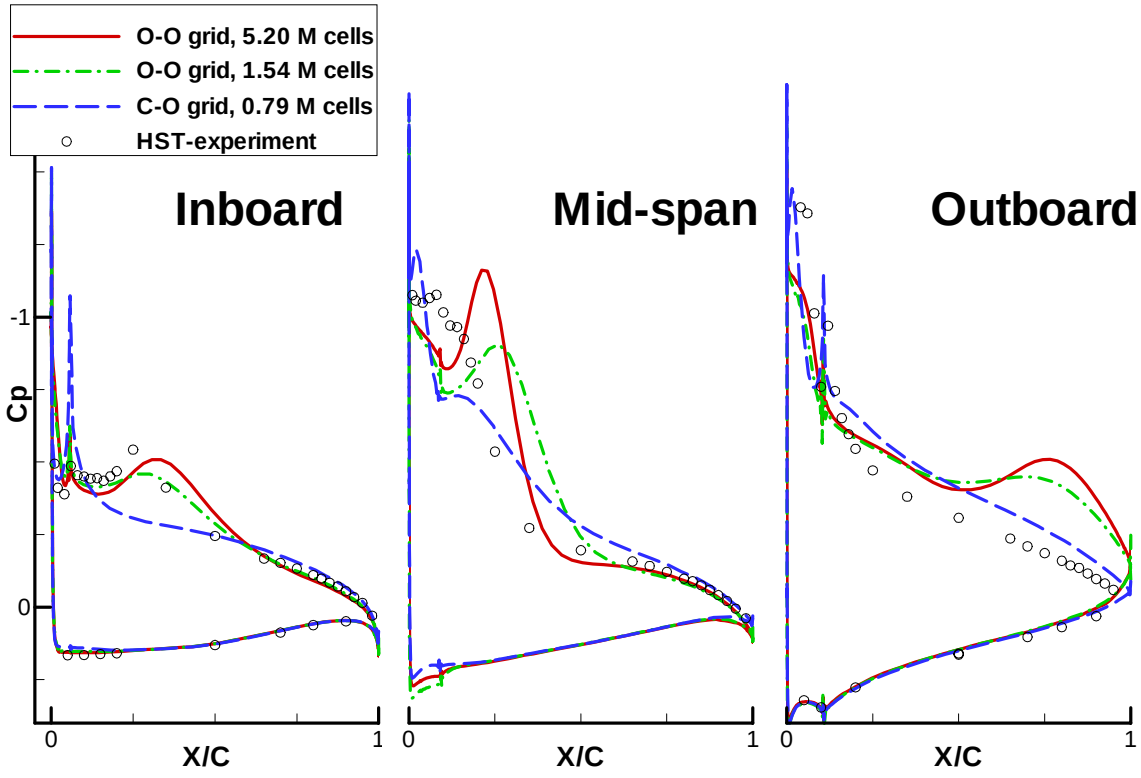

Fig 18 Pressure distribution, Ŭ = 9.5 degrees

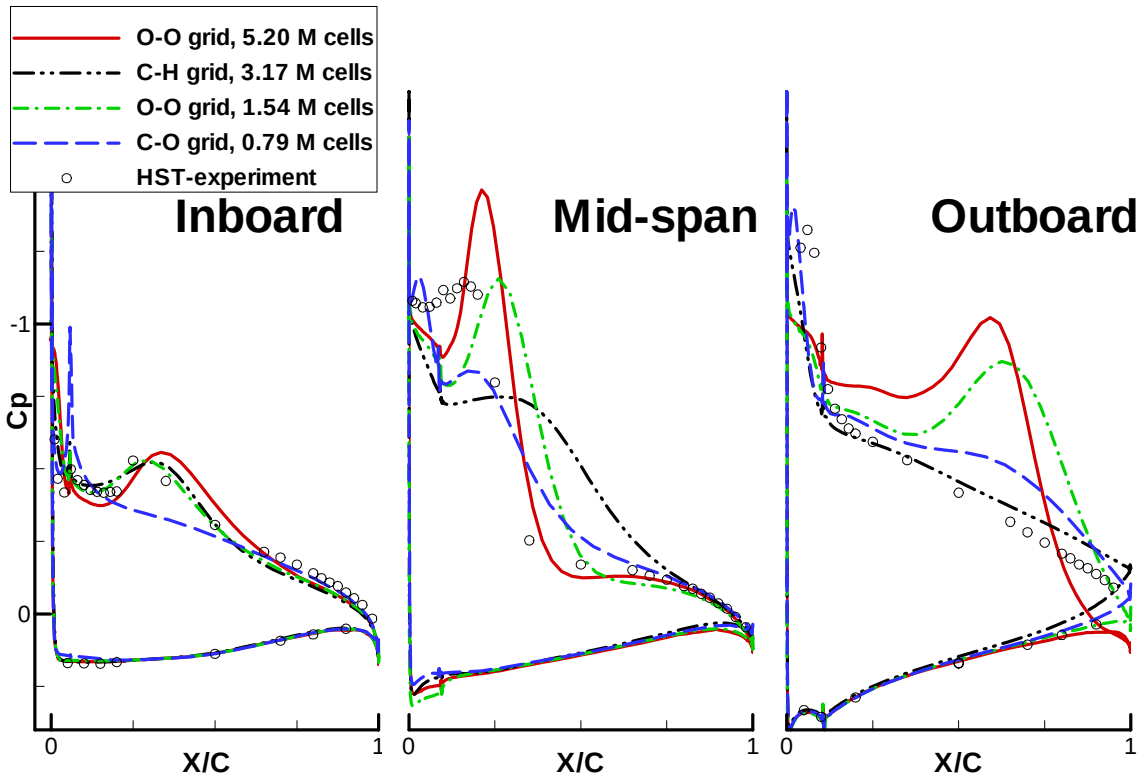

Fig 19 Pressure distribution, Ŭ= 10 degrees

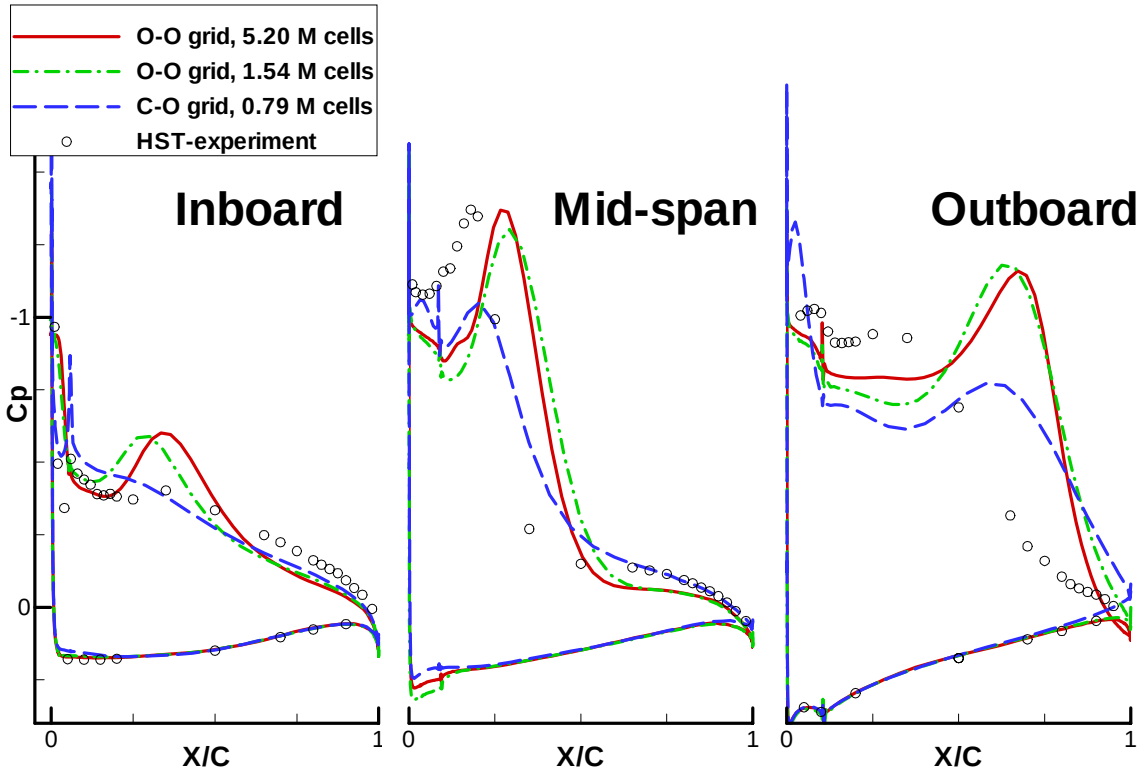

Fig 20 Pressure distribution, Ŭ= 10.5 degrees

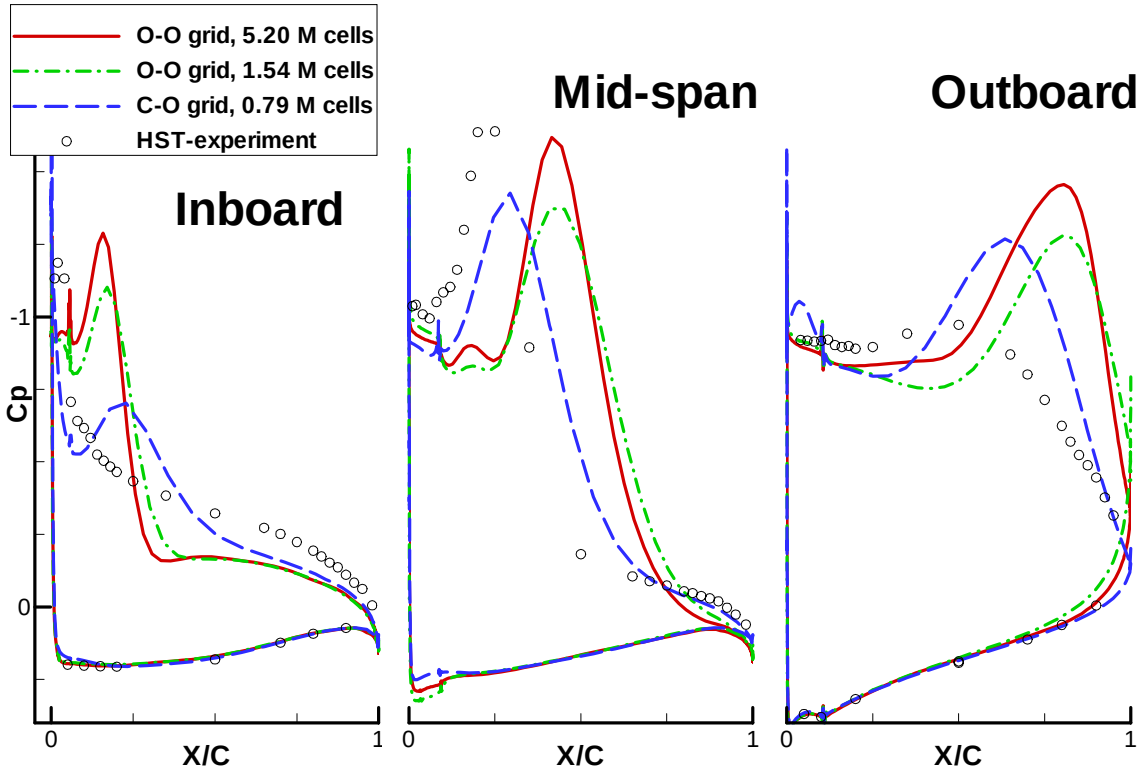

Fig 21 Pressure distribution, Ŭ = 12 degrees

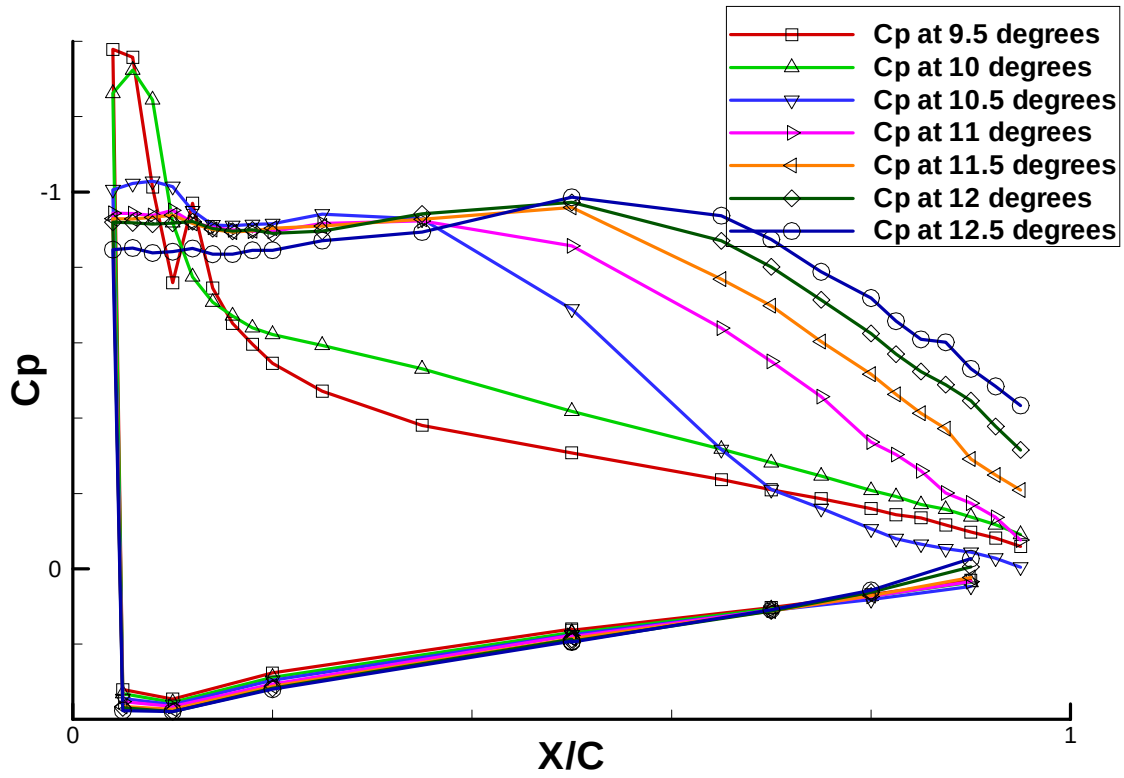

Fig 22 Development of experimental pressures with incidence at outboard wing section

The separation development as can be deduced from the CFD calculations has also been indicated in Fig 14. Basically, the same phenomena are observed, but at different incidences. Note that a local separation bubble might precede the separation either at the leading edge or at the ‘knuckle’; this is however more clearly detectable in the CFD skin friction lines. The available experimental information is insufficient to examine this phenomenon in more detail.

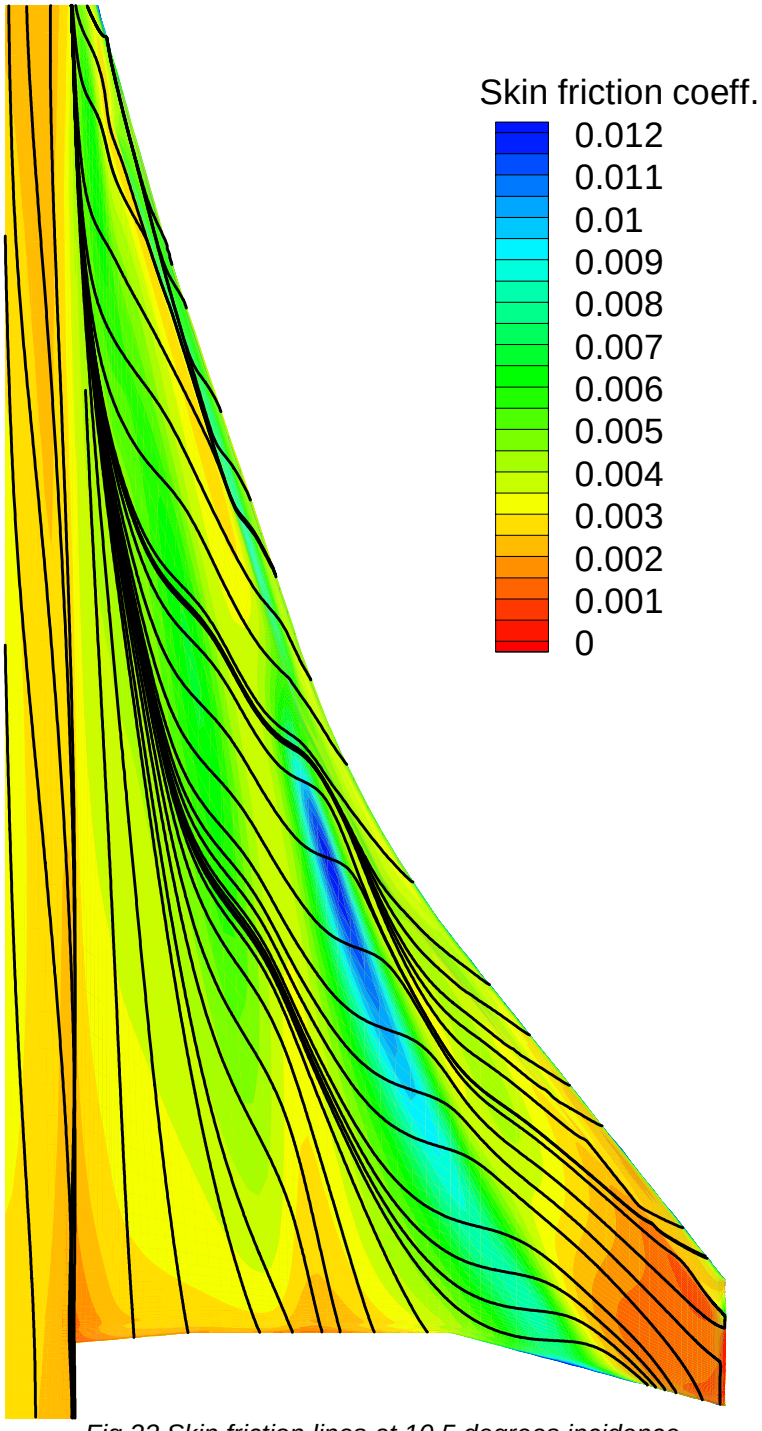

Fig 23 Skin friction lines at 10.5 degrees incidence

11 Comparison with CFD calculations: streamwise vortices

When comparing the experimental oil flows of Fig 12 with the calculated one in Fig 23 the occurrence of multiple vortices in the experiment represents a very noticeable difference. This can further be illustrated with the CFD calculated streamlines in the cross-flow plane (perpendicular to the free stream velocity) for (as a typical example) a spanwise section at 75% of the rootchord, also at 10.5 deg incidence (Fig 24). A weak inboard and a strong outboard vortex can be noticed. The corresponding flow topology 'types' for such a pair of vortices are sketched schematically in Fig 25. Note that the CFD-solution suggests a saddle point in the flow field instead of a separation and an attachment point on the wing surface in the experimental interpretation. The important difference is the absence of a separation line in the calculations cause of this difference. But there might also be a physical explanation. The vortex generated as a result of the large spanwise gradients near the 'knuckle' (inboard) or leading edge (mid-span) is convected downstream. On the wing surface, underneath this vortex, a pressure peak can be found that, when sufficiently strong, causes a kind of self-induced separation in the boundary layer on the wing surface, a bit similar to the more classical secondary separation underneath a vortex. This self-induced separation feeds the vortex that causes it! This is only possible when the vortex that is generated is sufficiently strong. The effect can only be reproduced in the calculations when the induced pressure gradient is accurately modeled (requiring a precise modelisation of the vortex itself) and when the turbulence model allows sufficient rotation of the velocity vector inside the boundary layer (that initiates the flow convergence and subsequently three-dimensional separation). In this respect it might be worthwhile to investigate the effects of more general turbulence models (e.g. explicit algebraic Reynolds stress modelling, EARSM) describing the three-dimensional turbulent flow in more detail than the presently used k-ω model.

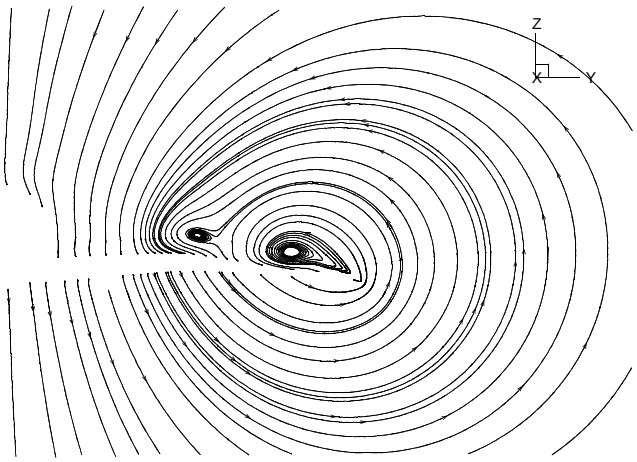

Fig 24 Streamlines in a cross-plane perpendicular to free-stream direction, Ŭ=10.5 degrees

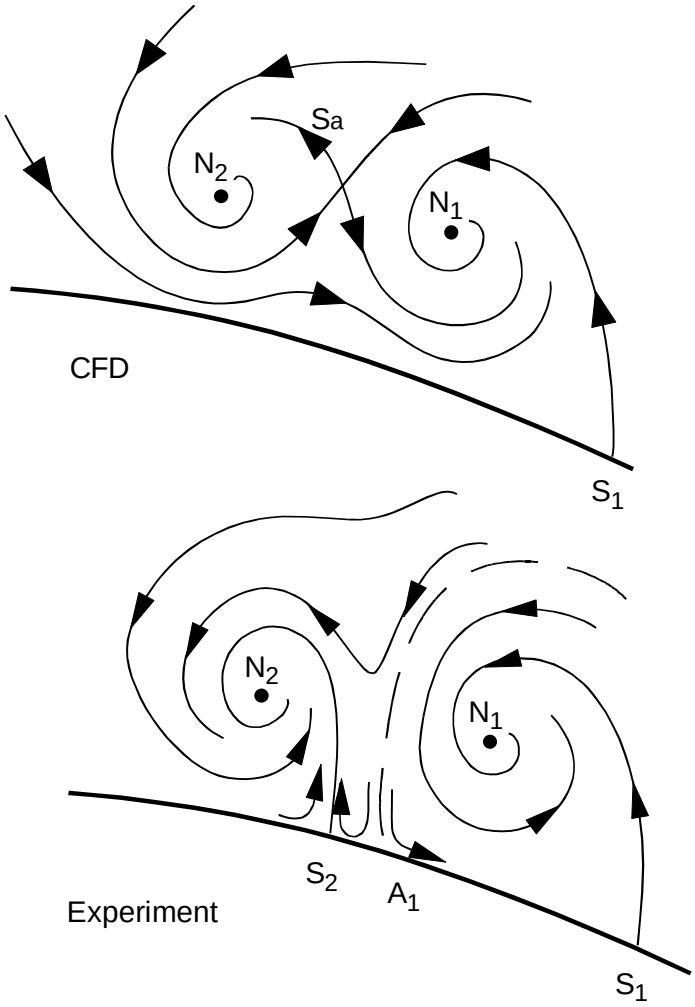

Fig 25 Vortical flow topology type differences between CFD and experiment at outer wing

This discussion does not explain the occurrence of multiple vortices as observed in Fig 12 through the related separation lines. Possible causes can be suggested, like partly separated flow on the flap, the discontinuities in the leading-edge geometry (due to the straight-segmented slat elements), or the formation of a stronger vortex (due to leading-edge separation) that pushes the existing weaker vortex away. It is also possible that the flow physics itself, due to the self- and mutually induced flow velocities, favors a multiple vortex system. The difference in flow topology at the wing tip between 10 and 10.5 degrees (Figs 12, 13) is an interesting illustration how a double vortex can change into a single one. Similarly, when looking more closely at the CFD skin friction lines of Fig 23, the mid-span wall streamlines just inboard of the leading edge appear to be close to separation (convergence). And finally, calculations with a C-H type mesh instead of an O-O type mesh suggest a possible triple vortex structure (Fig 11).

12 Prediction of aerodynamic coefficients

Aerodynamic coefficients, computed on the different meshes, are now compared with each other and with the experimental data. In the comparison, the industrial accuracy requirements are applied around the experimental data to indicate the acceptability range. The experimental data are taken from the EPISTLE test campaign, using the most effective transition strip. All computations were performed assuming a fully turbulent boundary layer. The small region of laminar flow at the leading edges will cause a slightly lower friction drag on the wind tunnel model for conditions with attached flow.

In Fig 26, the lift is shown as a function of incidence. The accuracy requirement with respect to incidence has been included. At moderate incidences, all computed results practically give identical lift coefficients that are in good agreement with experiment. At higher incidences, however, separation onset is encountered, visible as a transition in the experimental lift curve, and the associated vortex lift is seen to change the lift curve slope. Separation onset is not very accurately covered by coarse meshes, however acceptably predicted on the finer meshes. On all meshes, the change in lift curve slope appears to be overpredicted. This phenomenon has been identified as a shortcoming in the k-ϒ turbulence model corrections for vortex dominated flow, resulting in slightly too strong vortices (Ref 6).

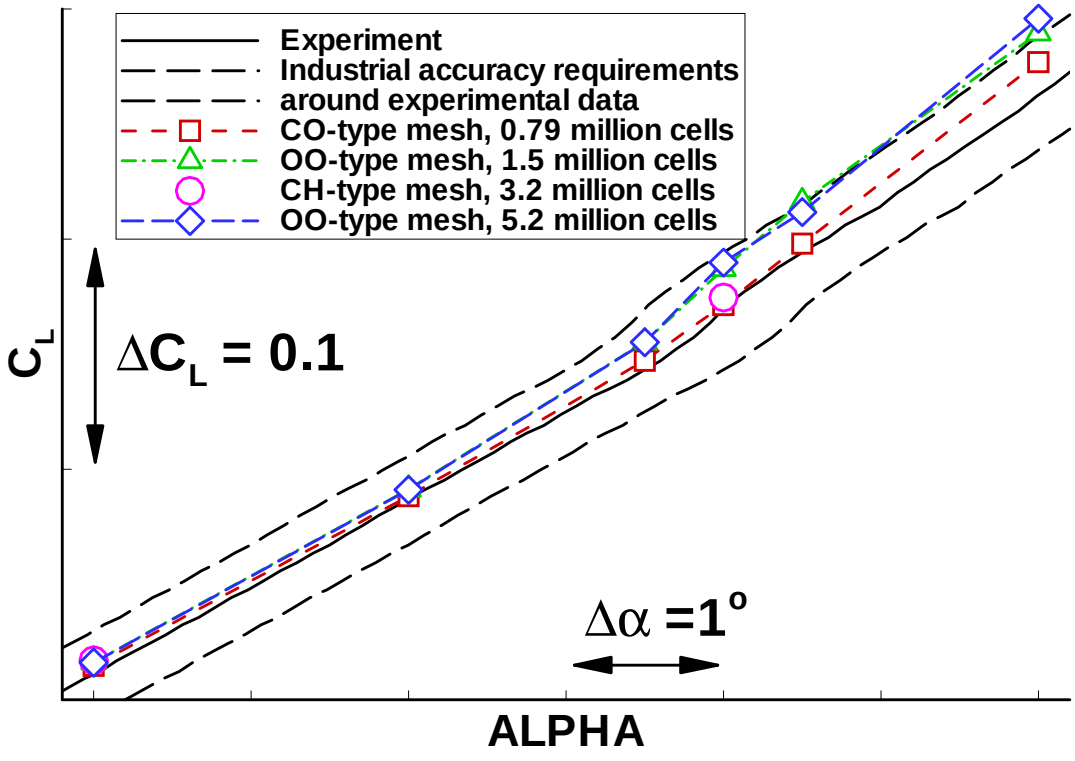

Fig 26 Comparison of computed and experimental lift curves

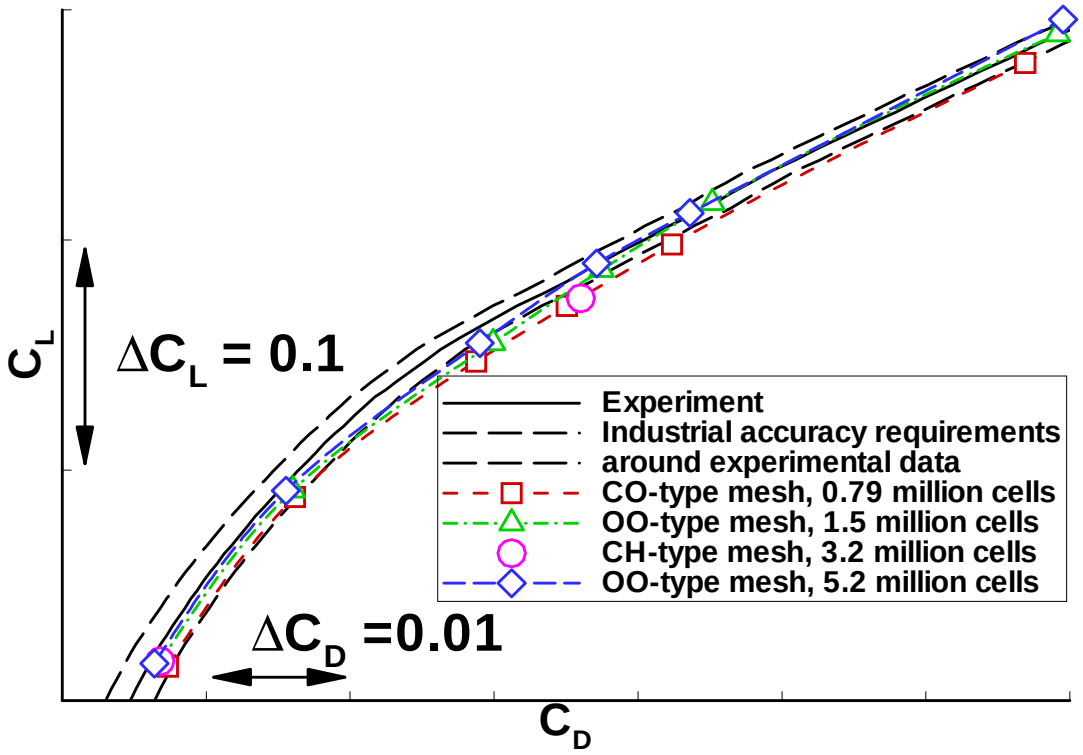

Fig 27 Comparison of computed and experimental drag polars

Drag polars are depicted in Fig 27. It is shown that the use of coarse meshes results in too high drag values that render the predicted polar outside of the acceptable range. The meshes with 1.5 million cells or more give results that are in better agreement with experiment over the full range examined.

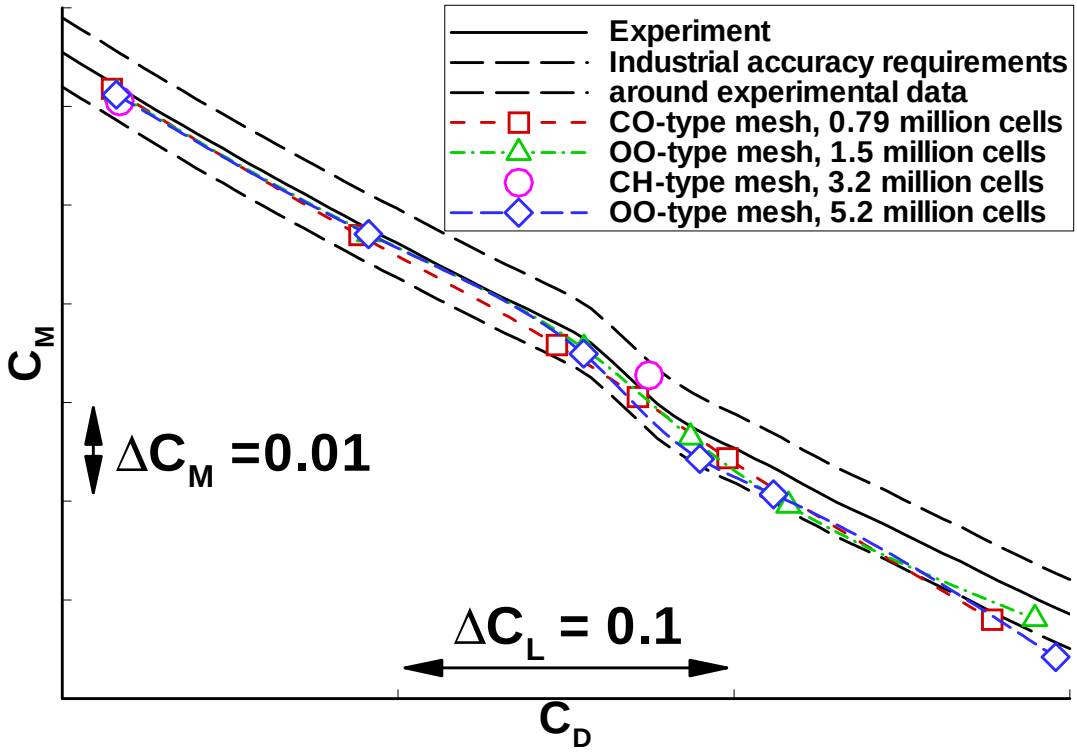

Fig 28 Comparison of computed and experimental pitching moment curves

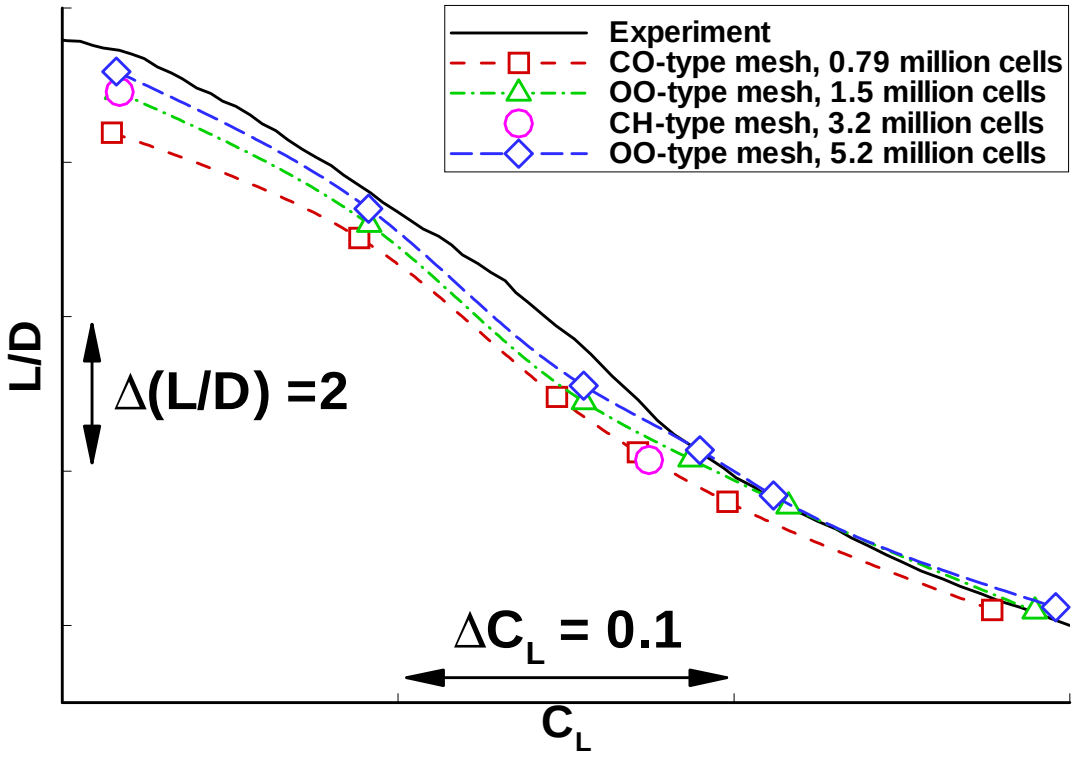

Fig 29 Comparison of computed and experimental aerodynamic efficiencies

Pitching moment curves are plotted in Fig 28. Very good agreement with experimental data is obtained at the low incidence range, almost independent of mesh density. This situation changes as soon as separation onset is encountered, resulting in more scatter in predicted values. It is shown that the transition phase at separation onset is more accurately captured on the finer meshes. Overall, the predicted pitching moment data are reasonably within the indicated acceptability range, even for separated conditions.

Finally, predicted lift-to-drag ratios, being the prime design variable for future configuration improvements, are examined in Fig 29. Due to its sensitivity to small differences in lift and drag, this parameter is indicative for minimum mesh density requirements. At moderate lift coefficients, the increase of cells in the computational meshes leads to a smaller difference with experimental data. A small difference, however, must remain due to the fully turbulent computations that differ from the experimental small laminar region ahead of the transition strips. At higher lift values, separations starting at the leading edge eliminate the effect of the small laminar region on drag, and the comparison with experiment is dominated by capturing sufficient details of the vortical flow.

Having now seen the performance of the present flow solver for this type of flow in terms of pressure distribution comparisons and predictions of aerodynamic coefficients, it is instructive to take notice of the results in Ref 11 where rather similar comparisons between theory and experiment for a comparable configuration are reported. Here, too, qualitatively reasonable agreement is found between theory and experiment, whereas in detail there are similar differences in especially outer wing vortex location for flow conditions containing separation.

It is concluded that, for a reliable prediction of aerodynamic coefficients within the accuracy ranges as indicated by industry, meshes of at least 1.5 million cells are needed. The use of such mesh resolutions is also recommended to be able to capture the nonlinear effects in the different coefficient curves, associated with separation onset.

13 Concluding remarks

Predictions of the low-speed flow around a complex SCT-configuration have been presented, based on k-γ turbulence modelling with specific modifications. Comparisons with experimental data lead to the conclusion that the flow around a SCT-configuration including complex separations can reasonably be predicted using present-day CFD-tools. When separations are present the mixed attached/separated flow is qualitatively reasonably well described and the resulting overall force and moment coefficients are still acceptable. However, details of the

CFD-solutions appear to depend on the mesh type and density. Some detailed flow features are not reproduced in the flow solutions like the generation of multiple streamwise vortices and the related separation lines on the surface (suggesting a kind of self-induced separation that feeds vorticity back into the respective vortex). It is argued that this shortcoming can be explained from deficiencies in turbulence modelling. A more detailed study of these effects, both for the vortex itself and for the three-dimensional boundary layer separation on the wing surface ('smooth separation') is recommended.
Although improvements in turbulence modelling would be welcome to assist the design process in more detail, the presented method can already successfully be applied to guide the improvement of the low-speed characteristics for an SCT design aiming at delaying separation onset and reducing separations.

Acknowledgements

This paper is partially based on results obtained within the European Project for the Improvement of Supersonic Transport Low-Speed Efficiency (EPISTLE). The cooperation with all partners in the EPISTLE project (Ref 3) and the support from the Commision of the European Union are gratefully acknowledged.

References

1. A.W. Wilhite and R.J. Shaw, *An Overview of NASA's High-Speed Research Program*, Proceedings of ICAS 2000, Paper 112.
2. D.A. Lovell, *European Research to Reduce Drag for Supersonic Transport Aircraft*, AIAA-99-3100.
3. U. Herrmann et.al., *Validation of European CFD Codes for SCT Low-Speed High-Lift Computations*, AIAA 2001-2405.
4. K.P. Nicholls, *Flap Systems on Supersonic Transport Aircraft*, Proceedings of ICAS 1996, Paper ICAS-96-4.4.4.
5. J.C. Kok, J.W. Boerstoel, A. Kassies and S.P. Spekreijse, *A Robust Multi-Block Navier-Stokes Flow Solver for Industrial Applications*, Proceedings of 3rd ECCOMAS Computational Fluid Dynamics Conference, Paris, 1996, also NLR-TP-96323.
6. F.J. Brandsma, J.C. Kok, H.S. Dol and A. Elsenaar, *Leading Edge Vortex Flow Computations and Comparison with DNW-HST Wind Tunnel Data*, Paper presented at RTO/ AVT Symposium on 'Vortical Flows and High Angle of Attack Aerodynamics', Loen, Norway, May 7th-11th, 2001, also NLR-TP-2001-238.
7. S.P. Spekreijse and J.C. Kok, *Semi-Automatic Domain Decomposition Based on Potential Theory*, Proceedings of the 7th International Conference on Numerical Grid Generation in Computational Field Simulations, Whistler, Canada, 25-28 September 2000, also NLR-TP-2000-366.
8. J. van Muijden and A. Elsenaar, *Transonic Aerodynamic Efficiency Assessment of an Optimised Supersonic Civil Transport Using CFD*, Proceedings of ECCOMAS 2000, Barcelona, 2000, also NLR-TP-2000-373.
9. B. Oskam and J.W. Slooff, *Recent Advances in Computational Aerodynamics at NLR*, AIAA-98-0138.
10. A. Elsenaar, *Vortex Formation and Flow Separation, the Beauty and the Beast in Aerodynamics*, The 2000 Lanchester Lecture, Aeronautical Journal of the Royal Aeronautical Society, December 2000.
11. F. Ghaffari, *Unstructured Grid Viscous Flow Simulation Over High-Speed Research Technology Concept Airplane at High-Lift Conditions*, NASA/TP-1999-209718.